

# High-OAM Deep Ultraviolet Twisted Light Generation for RF-Photoinjector Applications\*

A.S. Dyatlov<sup>1,2,†</sup>, D.M. Dolgintsev<sup>1</sup>, V.V. Gerasimov<sup>3,4</sup>, V.V. Kobets<sup>2</sup>, V.P. Nazmov<sup>3,5</sup>, M.A. Nozdrin<sup>2</sup>, A.N. Sergeev<sup>1</sup>, D.S. Shokin<sup>2</sup>, K.E. Yunenkov<sup>2</sup>, and D.V. Karlovets<sup>1,6</sup>

<sup>1</sup> *School of Physics and Engineering, ITMO University, 9 Lomonosova St., Saint-Petersburg, 191002, Russia*

<sup>2</sup> *Joint Institute for Nuclear Research, 6 Joliot-Curie St., Dubna, 141980, Moscow Region, Russia*

<sup>3</sup> *Budker Institute of Nuclear Physics, Siberian Branch of RAS, 11, Acad. Lavrentieva Pr., Novosibirsk, 630090, Russia*

<sup>4</sup> *Department of Physics, Novosibirsk State University, 1, Pirogova St., Novosibirsk, 630090, Russia*

<sup>5</sup> *Institute of Solid State Chemistry and Mechanochemistry, Siberian Branch of RAS, 18, Kutateladze St., Novosibirsk, 630090, Russia*

<sup>6</sup> *Petersburg Nuclear Physics Institute of NRC "Kurchatov Institute", 1, mkr. Orlova roshcha, Gatchina, Leningradskaya Oblast, 188300, Russia*

## Abstract

We report on the generation and characterization of ultraviolet (the wavelength of 266 nm) twisted light with a high orbital angular momentum (OAM) using three types of fabricated diffractive optical elements (DOEs): a reflective fork grating, a high-charge spiral phase plate (SPP), and binary axicons. All elements were integrated into a drive-laser beamline of an electron RF-photoinjector, enabling direct evaluation under accelerator-relevant conditions.

The SPP produced a high-purity Laguerre–Gaussian mode with the OAM  $\ell = 64$  and a measured conversion efficiency of 80%. Binary axicons generated quasi–Bessel twisted light with the topological charges up to  $m = 10$ , exhibiting low divergence and stable multi-lobe ring structures. The fork grating reliably produced lower-order modes,  $\ell = 2–8$ , with a good agreement between simulations and cylindrical-lens diagnostics.

These results constitute, to our knowledge, the first comprehensive experimental demonstration of deep-UV high-OAM beams generated with fabricated DOEs and validated through mode-conversion measurements. The demonstrated techniques are compatible with high-power UV laser systems used in RF-photoinjectors and offer a practical route toward structured photocathode illumination and the generation of relativistic vortex electron at a particle accelerator facility.

## 1 Introduction

Optical beams of the so-called twisted light [2, 3, 4, 5, 6, 7, 8, 9, 10], carrying orbital angular momentum (OAM) play an increasingly important role in modern photonics, enabling advanced control of light–matter interactions [11], high-dimensional quantum communication protocols [12, 13, 14], and structured-beam excitation in electron and plasma systems [15]. Generating well-defined OAM modes in the deep ultraviolet

\*This document is the results of the research project funded by the Russian Science Foundation (Project No. 23-62-10026) [1]

†email: [aleksandr.dyatlov@metalab.ifmo.ru](mailto:aleksandr.dyatlov@metalab.ifmo.ru)

(UV) range is particularly relevant for photocathode-based electron sources [5, 7, 8, 9, 16] and nonlinear UV photonics, where high spatial coherence, low divergence, and precise transverse-mode control are required.

However, producing stable high-charge OAM beams in the deep UV remains technically challenging. Spatial light modulators and digital micromirror devices, widely used at visible wavelengths, suffer from strong absorption, laser-induced damage, and low diffraction efficiency in the UV range. Binary spiral zone plates (SZPs) operate in this spectral range but are intrinsically limited to about 40% conversion efficiency [17]. Classical fork gratings [18] can offer higher efficiency, yet they restrict the accessible OAM values to integer multiples of the diffraction order and often require tight focusing. Spiral phase plates (SPPs), while conceptually ideal for generating arbitrary OAM values [19], demand nanometer-scale surface accuracy over millimeter-sized apertures [20] and must withstand significant UV fluence. Binary axicons, widely used to generate Bessel-like twisted light (vortex) [21, 22, 23], provide robustness and tunability but introduce characteristic ring fragmentation due to their discretized phase profiles. As a consequence, none of these approaches alone provides a universal, high-fidelity, UV-compatible solution for high-order OAM generation.

In this work, we demonstrate ultraviolet twisted light generation using three fabricated diffractive optical elements (DOEs): reflective fork gratings, high-charge spiral phase plates, and binary axicons, all integrated into a drive-laser system of an RF-photoinjector [24]. We generate Laguerre–Gaussian (LG) modes with the OAM values up to  $\ell = 64\hbar$ , verify their modal structure using cylindrical-lens mode conversion, and compare the measured intensity distributions with numerical simulations. The generated beams exhibit high spatial fidelity, stable operation under UV irradiation, and low divergence suitable for photocathode illumination. The fabrication techniques used here rely on robust, scalable processes compatible with fused silica, SU-8 resists, and metal-coated substrates, enabling durable large-aperture UV optics.

To the best of our knowledge, this is the first comprehensive experimental demonstration of the deep-UV high-OAM beams produced using fabricated DOEs and validated through the mode-conversion diagnostics. These results are directly relevant for the next-generation accelerator facilities. Relativistic vortex electrons are attracting increasing interest in nuclear and hadronic physics, where OAM offers a new degree of freedom for probing spin-structure phenomena and may complement the conventional spin-polarized beams [7, 9, 25, 26, 27]. Structured photocathode illumination is likewise becoming important for accelerator-based light sources, including polarized synchrotron-radiation facilities, free-electron lasers, and Compton  $\gamma$ -ray sources, all of which benefit from precise control of the transverse phase space of the injected electrons. The demonstrated deep-UV high-OAM beam generation thus can provide [1] a practical route toward the realization of MeV-scale vortex electrons in modern high-brightness photoinjectors.

## 2 Design and Fabrication of High-OAM Diffractive Optical Elements

### 2.1 A Reflective Diffraction Fork Grating with a Topological Charge $m = 2$

A fork grating introduces a phase dislocation of topological charge  $m$ , generating optical vortices in the diffracted orders. The phase profile employed in this work follows Ref. [2]:

$$\Phi(x, y) = 2\pi \frac{x}{x_0} + m \arctan \frac{y}{x}, \quad (1)$$

where  $x_0$  denotes the grating period. The continuous phase distribution is converted into a binary mask by applying a cosine-based threshold function,

$$B(x, y) = \begin{cases} 1, & M(x, y) > T, \\ 0, & M(x, y) \leq T. \end{cases} \quad (2)$$

with the modulation function defined as

$$M(x, y) = \frac{1}{2} \alpha [1 + \cos \Phi(x, y)]. \quad (3)$$

In this context, the topological charge of the grating  $m$  is the number of  $2\pi$  phase windings embedded into the grating period. When a Gaussian beam is diffracted, each diffraction order acquires an optical vortex with topological charge of the beam [28]

$$\ell = n \cdot m. \quad (4)$$

where  $n$  is the diffraction order. The vortex charge  $\ell$  defines the OAM carried by the beam, with each photon transferring  $\ell\hbar$  of the OAM.

The resulting binary mask is shown in Fig. 1. The pattern was transferred onto an aluminum mirror via laser engraving, yielding a reflective grating with a  $1 \times 1$  mm active area and a spatial resolution of approximately  $30 \mu\text{m}$ . A microscope image of the fabricated device is presented in Fig. 2.

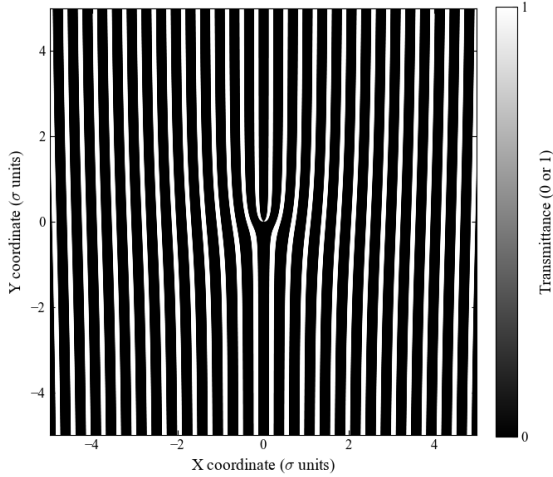


**Figure 1:** A binarized fork-grating mask.

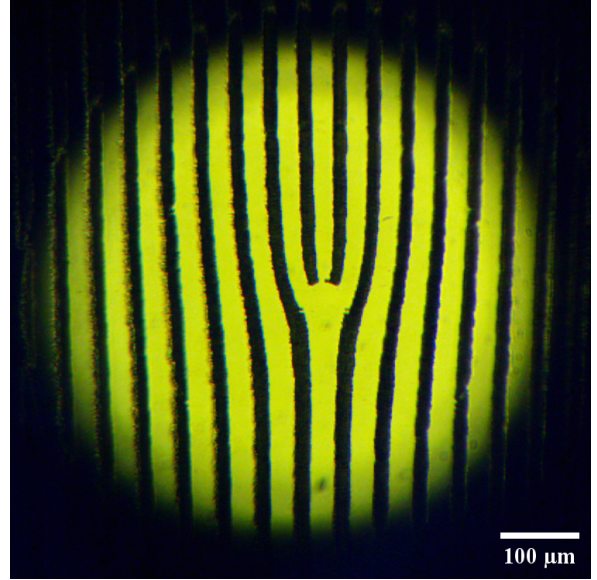


**Figure 2:** A microscope image of the fork grating.

## 2.2 A Spiral Phase Plate with a Topological Charge $m = 64$

A spiral phase plate (SPP) generates an azimuthally varying phase through a helical surface relief. The phase shift introduced by the plate is given by [20]

$$\varphi_0(\theta) = \frac{2\pi}{\lambda} \left[ (n - n_0) \frac{h_s \theta}{2\pi} + n h_0 \right], \quad (5)$$

where  $n$  and  $n_0$  are the refractive indices of the plate material and the surrounding medium, respectively;  $h_0$  is the base thickness;  $h_s$  is the total height variation over a full  $2\pi$  rotation; and  $\theta$  is the azimuthal angle. The corresponding surface profile is

$$h(\theta) = h_s \frac{\theta}{2\pi} + h_0. \quad (6)$$

To generate a twisted light with an OAM  $\ell$ , the phase must increase by  $2\pi m$  over one full revolution:

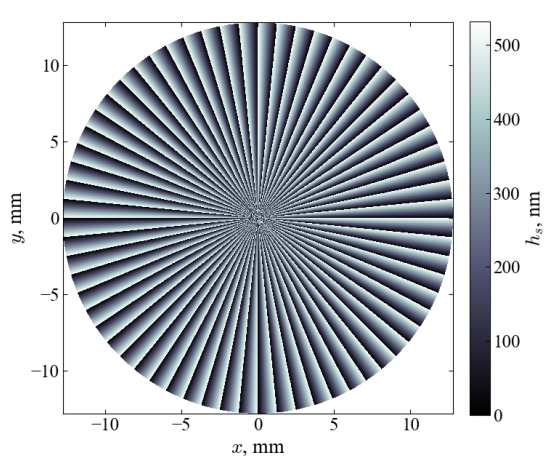
$$\varphi_0(\theta) = \ell\theta + \frac{2\pi n h_0}{\lambda}. \quad (7)$$

For UV operation at  $\lambda = 266$  nm using fused silica ( $n = 1.49$ ), the required total height variation is approximately  $h_s \approx 34 \mu\text{m}$ . Implementing a topological charge of  $m = 64$  is achieved by dividing the spiral into 64 discrete azimuthal sectors, each introducing a  $2\pi$  phase step. This corresponds to a height increment of about 532 nm per sector. The resulting two-dimensional phase topology is shown in Fig. 3.

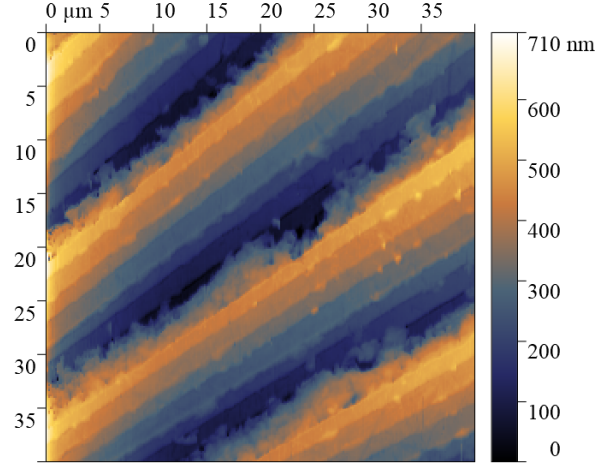
The SPP was fabricated in fused silica using multi-level photolithography followed by high-precision plasma etching (Holo/Or, Israel). This manufacturing process is commonly employed for diffractive optical elements and provides the required micron-scale surface relief and sub-micron accuracy of the phase profile, ensuring stable performance under high-intensity UV illumination [29, 30, 31, 32].

Figure 4 shows the measured surface profile of the fabricated SPP obtained using an AIST-NT SmartSPM 1000 atomic force microscope (AFM). The AFM image reveals that small dust particles accumulated inside the narrow gaps between adjacent sectors during handling, although this contamination

did not affect the quality of the generated twisted light. A weak striped pattern is also visible across the sectors, originating from layer-by-layer etching into the fused-silica substrate. Despite this fine structuring, the average step height remains close to 500 nm, which is in good agreement with the designed two-dimensional topological phase map.



**Figure 3:** Two-dimensional phase topology of the spiral phase plate (SPP) featuring 64 azimuthal steps within an aperture of  $D = 25.6$  mm. The topological charge is  $m = 64$ . The step height is  $h_s \approx 532$  nm, calculated for  $\lambda = 266$  nm and  $n = 1.49$ .



**Figure 4:** The atomic force microscope image of the fabricated SPP. Dust particles trapped between the etched sectors and the striped etching pattern do not degrade the beam quality. The measured step height is  $\sim 500$  nm, consistent with the design.

### 2.3 Axicons with the Topological Charge $m = 3$ and 10

Bessel beams were modeled using the Wave-ThruMasks MATLAB package [33], which computes field propagation through transparent phase elements within the scalar diffraction theory using the Rayleigh–Sommerfeld integral [34]. The binary phase distribution used to generate twisted light Bessel beams is

$$H(r, \varphi) = F(\ell\varphi - kr) = \frac{\pi}{2} \times \text{sign}[\sin(m\varphi - kr)], \quad (8)$$

where  $m$  is the topological charge,  $\varphi$  the azimuthal angle,  $k$  the radial wave number, and  $r = \sqrt{x^2 + y^2}$ . An example mask for  $m = 3$  is shown in Fig. 5(a).

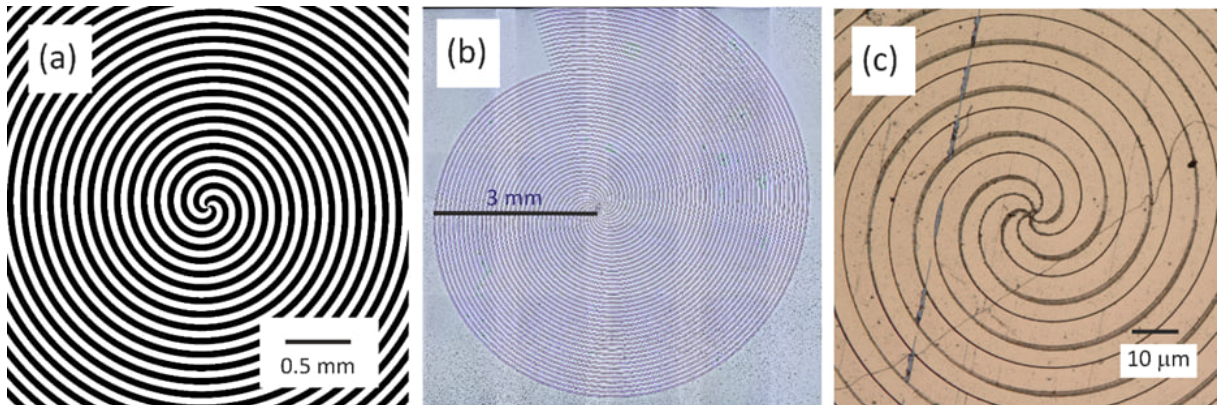


**Figure 5:** (a) Phase mask of an axicon with topological charge  $m = 3$ . The micrograph of a binary planar axicon with an aperture diameter of 6 mm and  $m = 3$  in a SU-8 photoresist layer; (b) full view; (c) enlarged view obtained in refractive mode, covered with a gold layer

Binary axicon topologies in the form of Archimedean spirals with  $m = 3$  and  $m = 10$  and a period of  $p = 100 \mu\text{m}$  were generated in MathCad. The rendering process was terminated once the spirals reached the working aperture of 6 mm.

The encoded topology was first transferred onto a glass photomask in an iron-oxide layer. The axicons were then fabricated via photolithography in SU-8 photoresist deposited on leucosapphire substrates, which provide high ultraviolet transmittance. The polymer crosslinked network of SU-8 also offers high resistance to ionizing radiation [35]. Prior to resist deposition, the substrates were cleaned sequentially in acetone and in a 5% aqueous sulfuric-acid solution. To achieve the required film thickness, SU-8 2002 resist was diluted with SU-8 2000 Thinner.

The required binary layer thickness is

$$h = \frac{\lambda}{2(n-1)}, \quad (9)$$

where  $n \approx 1.66$  is the refractive index of SU-8. For  $\lambda = 266 \text{ nm}$ , this yields  $h \approx 200 \text{ nm}$ , providing the necessary  $\pi$  phase shift.

The photoresist was applied using a spin coater operated at 3000 rpm. The resulting film was soft-baked on a hotplate at  $95^\circ\text{C}$  for 5 minutes. The axicon pattern was transferred using a custom UV exposure system based on an H44TV1C0-LFVY LED lamp operating at a wavelength of 365 nm, with an exposure time of 23 minutes. After a post-exposure bake at  $95^\circ\text{C}$  for 5 minutes and development for 1.5 minutes in PGMEA, the resist thickness was measured with a Linnik MII-4 interference microscope with an accuracy of  $\pm 15 \text{ nm}$ . Figures 5(b-c) show the resulting axicon relief.

### 3 Numerical Modeling of the Generated Beams

Numerical simulation of the fork grating and the SPP was performed using a standard angular-spectrum propagation framework [34]. The incident field was taken to be a Gaussian beam,

$$E_G(x, y) = E_0 \exp\left[-\frac{x^2 + y^2}{w_0^2}\right], \quad (10)$$

where  $x$  and  $y$  are the transverse coordinates,  $w_0$  is the initial beam waist, and  $E_0$  is the input field amplitude. This field was multiplied by the corresponding DOE phase:  $\Phi(x, y)$  from Eq. 1 for the fork grating and  $\varphi_0(\theta)$  from Eq. 5 for the SPP:

$$E_{\text{fork}}(x, y) = E_G(x, y) \exp[i\Phi(x, y)], \quad (11)$$

$$E_{\text{SPP}} = E_G(x, y) \exp[i\varphi_0(\theta)] A(R). \quad (12)$$

To suppress boundary artifacts and mitigate residual on-axis intensity that appear in high-charge modes, an apodization function was introduced:

$$A(R) = \exp\left[\left(\frac{R}{R_0}\right)^p\right] \cdot \left(1 - \exp\left[\left(\frac{R}{R_C}\right)^q\right]\right), \quad (13)$$

where  $R = \sqrt{x^2 + y^2}$ ,  $R_0$  defines the outer truncation radius, and  $R_C$  specifies the central suppression zone.

Free-space propagation was computed using the angular-spectrum method,

$$E(x, y, z) = \mathcal{F}^{-1}\{\mathcal{F}[E(x, y)]H_{\text{prop}}(f_x, f_y, z)\}, \quad (14)$$

where  $\mathcal{F}$  and  $\mathcal{F}^{-1}$  denote the forward and inverse 2D Fourier transforms,  $f_x$  and  $f_y$  are the spatial frequencies, and the transfer function is

$$H_{\text{prop}}(f_x, f_y, z) = \exp[-i\pi\lambda z(f_x^2 + f_y^2)], \quad (15)$$

When a lens was included, its quadratic phase was applied in the Fourier domain, after which the field was propagated to the observation plane using the same operator. The resulting optical intensity distributions were computed as

$$I(x, y) = |E_{\text{out}}(x, y)|^2, \quad I_{\text{norm}}(x, y) = \frac{I(x, y)}{I_{\text{max}}(x, y)}. \quad (16)$$

This modeling procedure enables direct comparison between the fork-grating-generated and SPP-generated beams, including verification of the expected OAM values. The simulated output patterns are shown in Figs. 6 and 7.

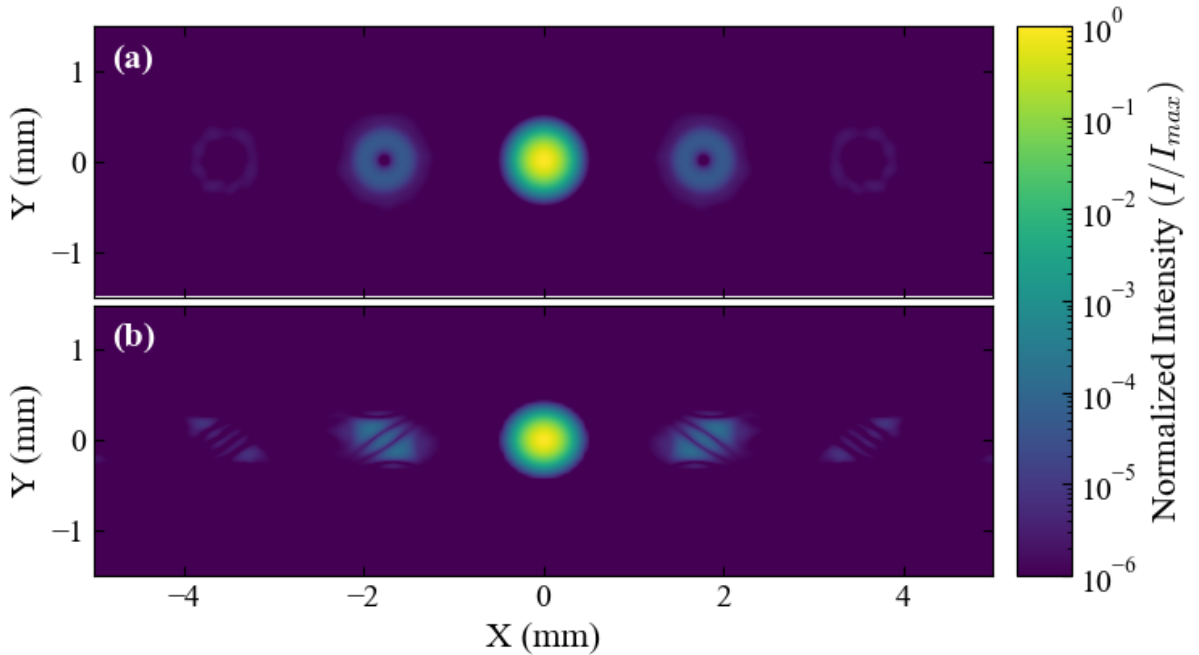


**Figure 6:** Simulation of the twisted light generation using the fork grating. (a) Transformation of the Gaussian input into the Laguerre–Gaussian modes carrying the OAM  $\ell = 0, \pm 2, \pm 4$ . (b) Corresponding cylindrical-lens mode conversion into the Hermite–Gaussian modes of the orders  $N = 1, 3, 5$ .

Similarly to the Laguerre–Gaussian simulations, quasi–Bessel beams produced in the focal region of the fabricated axicons were numerically modeled following the methodology of Ref. [23]. The results are shown in Fig. 8. For all topological charge values, the characteristic ring-shaped intensity distribution is reproduced, consisting of  $m$  localized bright lobes whose number corresponds to the topological charge of each axicon. Small parasitic background features appear as weak spiral-like artifacts.

We also note that the binary phase pattern can lead to an effective interference of several overlapping wave components carrying slightly different OAMs. In this interpretation, the quasi–Bessel field can be viewed not as a single-mode vortex, but as a superposition of nearby OAM states [36, 37, 38]. The average topological charge would still correspond to the design value  $m$ , while the OAM can exhibit a finite dispersion, defining an effective OAM bandwidth. This qualitative picture is consistent with the observed fragmented ring structure and is commonly discussed for binary axicons.

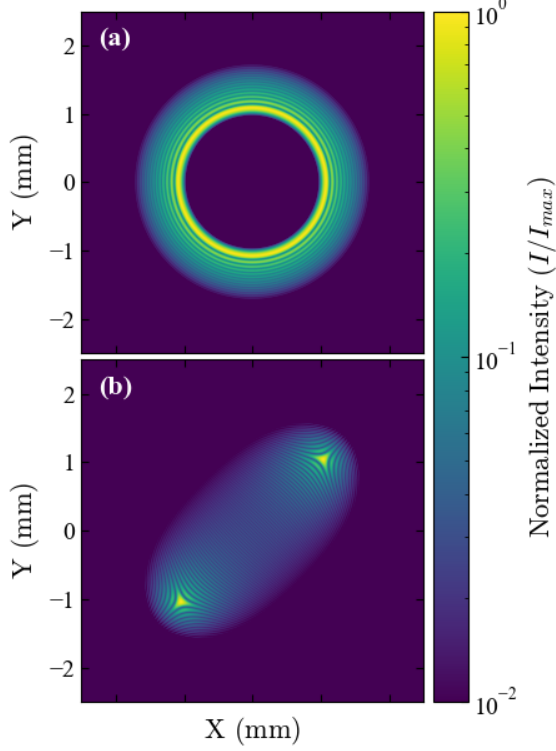
In contrast, an ideal (non-binary) axicon produces a continuous, smooth ring [21]. In the present case, the discretization inherent to the binary phase patterns results in a fragmented ring composed of distinct intensity maxima, consistent with the expected behavior of binary axicons.

## 4 Experimental Results and Beam Imaging

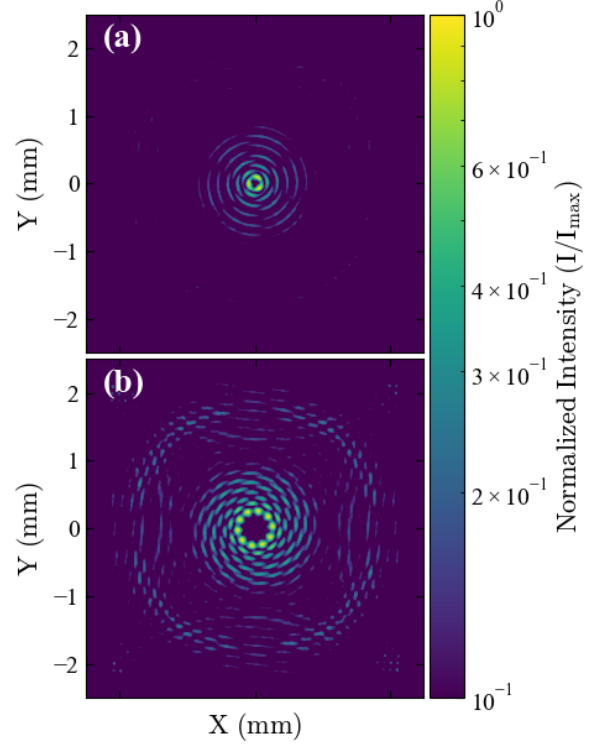
### 4.1 Experimental Setup

Figure 9 shows the optical setup used to characterize the fabricated DOEs. The ultraviolet beam at the wavelength of  $\lambda = 260\text{--}266\text{ nm}$  was extracted from the photoinjector transport line using a secondary periscope and then directed through a spatial filter composed of lens L1 ( $f_1 = 220\text{ mm}$ ) and a  $200\text{ }\mu\text{m}$  pinhole. For measurements involving the fork grating, an additional lens L2 was inserted to provide tighter focusing onto the DOE.

After spatial filtering, the beam illuminated the DOE under test (fork grating, SPP, or axicon). For the OAM diagnostics in the fork-grating and SPP experiments, a cylindrical lens with focal length  $f_{\text{cyl}} = 100\text{ mm}$  was used to perform Laguerre–Gaussian to Hermite–Gaussian (LG-to-HG) mode conversion [39, 40]. The resulting intensity patterns were recorded using a UV-sensitive SDU-285R CCD camera.



**Figure 7:** Simulation of twisted light generation using the designed SPP. (a) Transformation of a Gaussian input into the Laguerre-Gaussian mode carrying the OAM  $\ell = 64$ . (b) Cylindrical-lens conversion into the corresponding Hermite-Gaussian mode of the order  $N = 65$ .



**Figure 8:** Simulated quasi-Bessel beams generated by binary axicons with topological charges  $m = 3$  and  $10$  (left to right). Each pattern exhibits an  $m$ -lobe intensity ring, while the binary phase structure leads to a segmented rather than continuous ring profile.

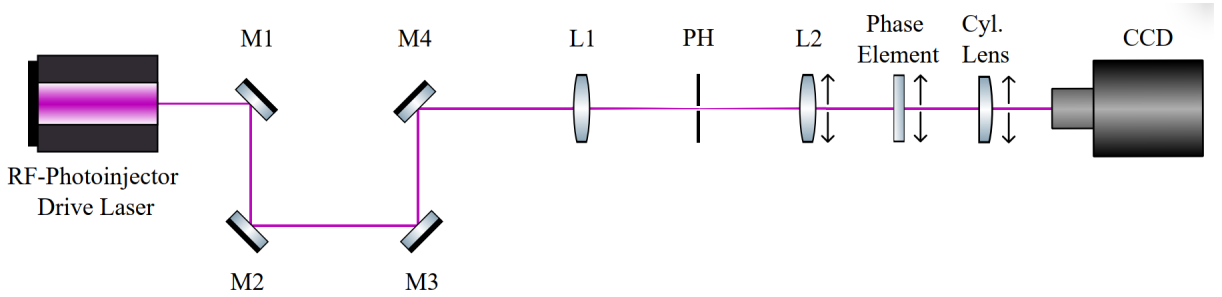


**Figure 9:** Schematic layout of the experimental setup. The system includes the RF photoinjector drive laser; periscope mirrors M1-M2 (beam extraction) and M3-M4 (beam transfer); spatial-filtering lens L1 and pinhole PH; optional lens L2 for fork-grating measurements; the tested phase element (fork grating, SPP, or axicon); a cylindrical lens for the OAM diagnostics; and a UV-sensitive CCD camera for beam imaging.

This optical layout also enables the formation of a Gaussian beam with a transverse diameter of approximately  $800 \mu\text{m}$  and low angular divergence, suitable for subsequent illumination of photocathodes or additional diagnostics.

## 4.2 Experiments with Fork Grating

The reflective fork grating was first tested using the UV beam prepared by the spatial-filtering stage. The generated twisted light are shown in Fig. 10. In these measurements, the central (zeroth-order) beam was blocked to avoid saturation of the CCD sensor. As expected for a grating with  $m = 2$ , the  $\pm 1$  and  $\pm 2$  diffraction orders produced Laguerre-Gaussian modes with orbital angular momenta  $\ell = \pm 2$  and  $\ell = \pm 4$ , respectively.

Power measurements using an Ophir 3A-FS detector confirmed that the majority of the transmitted

energy was contained in the zeroth and first diffraction orders, while higher orders carried progressively smaller power fractions.

The corresponding Hermite–Gaussian modes obtained after cylindrical-lens conversion are presented in Fig. 10(b). The observed modal structures agree with the expected relation [39, 40]

$$N = |\ell| + 1, \quad (17)$$

demonstrating that the grating reliably generates the targeted OAM states. Higher diffraction orders ( $n = -3$  and  $n = -4$ ), shown in Fig. 11, also exhibit well-defined modal patterns, confirming correct operation of the fabricated structure across multiple orders.

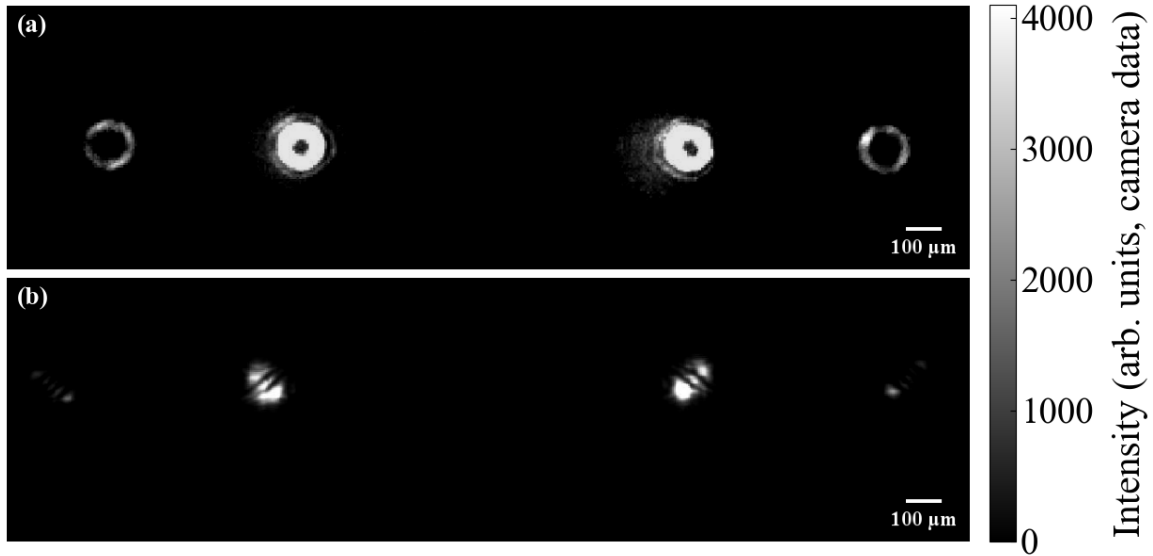


**Figure 10:** Twisted light generated by the reflective fork grating for diffraction orders  $\pm 1$  and  $\pm 2$ . (a) Laguerre–Gaussian modes with the OAM  $\ell = \pm 2$  and  $\ell = \pm 4$ . (b) Corresponding Hermite–Gaussian modes obtained after cylindrical-lens mode conversion.

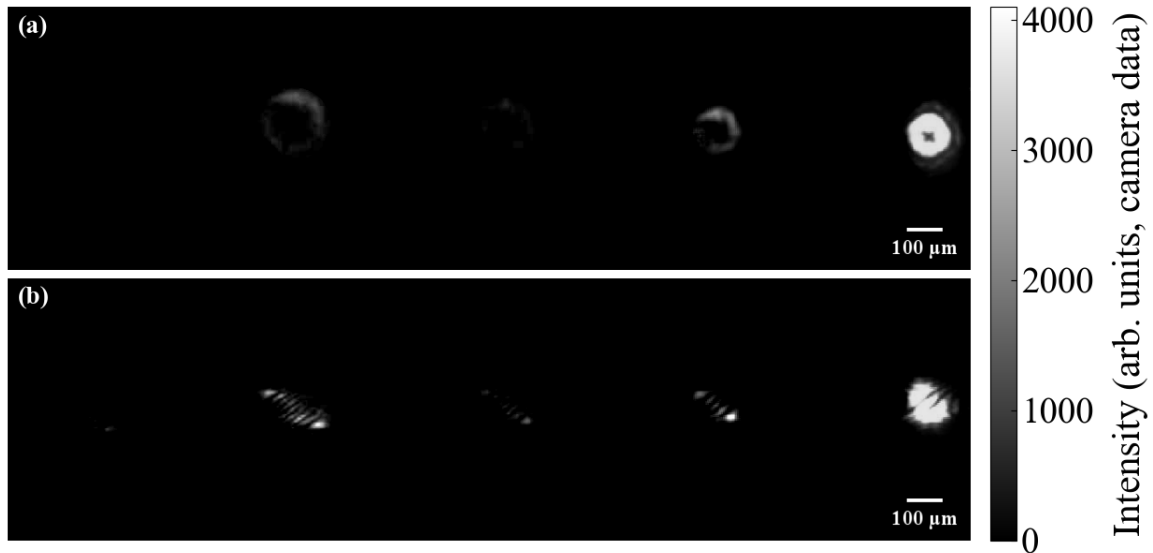


**Figure 11:** Higher-order twisted light generated by the reflective fork grating. (a) Laguerre–Gaussian modes with the OAM  $\ell = -2, -4, -6, -8$  observed in the  $n = -1, -2, -3,$  and  $-4$  diffraction orders. (b) Corresponding Hermite–Gaussian modes obtained after cylindrical-lens mode conversion.

A potential route for improving the performance of the diffractive element is to increase the spatial resolution of the grating lines. A finer grating would enable generation of higher-quality vortex modes but would also require tighter focusing of the incident beam onto the grating surface. Overall, the experimentally measured spatial profiles in Fig. 10 show good qualitative agreement with the simulations presented in Fig. 6, confirming correct operation of the fabricated fork grating.

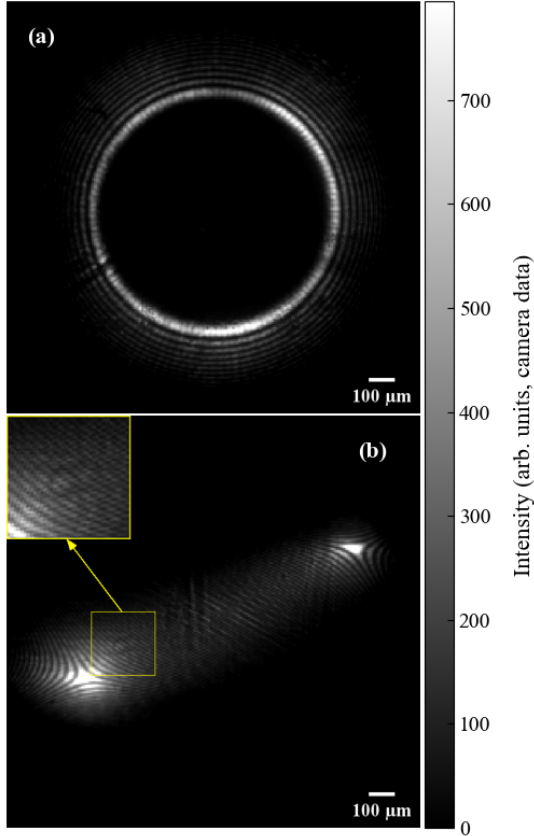


**Figure 12:** Twisted light generated by the SPP. (a) Laguerre–Gaussian vortex carrying the OAM  $\ell = 64$ . (b) Corresponding Hermite–Gaussian mode of the order  $N = 65$  obtained after cylindrical-lens mode conversion.

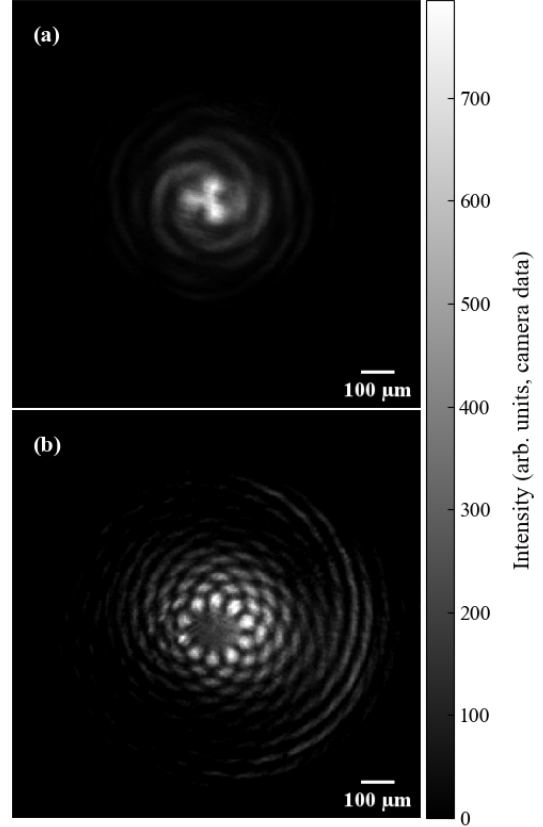


**Figure 13:** Twisted light generated by the binary axicons. (a) Quasi–Bessel beam produced by the axicon with the topological charge  $m = 3$ , exhibiting three intensity lobes. (b) Quasi–Bessel beam produced by the axicon with the topological charge  $m = 10$ , exhibiting ten resolved lobes.

### 4.3 Experiments with SPP

The next experiment was performed using the fabricated SPP, and the resulting beam profiles are shown in Fig. 12. The output twisted light (Fig. 12(a)) exhibits a well-defined annular structure with a pronounced central singularity. A portion of the beam energy is redistributed into several weak concentric rings surrounding the primary vortex mode, consistent with the expected behavior of high-charge SPP-generated beams.

Power measurements performed with the Ophir 3A-FS detector showed an intensity reduction of approximately 20%. Although this differs from the theoretical conversion efficiency of  $\sim 90\%$ , the obtained value is still reasonable given the surface-profile discretization, potential scattering losses, and alignment constraints in the UV. The measured twisted light structure and transverse size closely match the simulated pattern shown in Fig. 7.

The Hermite–Gaussian mode exhibits a slightly larger tilt compared with the simulation. This effect is attributed to a small intentional misalignment of the beam relative to the focal plane of the cylindrical lens, introduced to improve the separation and visibility of the experimentally observed mode stripes.

### 4.4 Experiments with Axicons

The final series of experiments was performed using the fabricated binary axicons. The resulting quasi-Bessel beams are shown in Fig. 13. For the axicon with the topological charge  $m = 3$  (Fig. 13(a)), three intensity lobes are clearly visible, consistent with the expected topological charge. At short propagation distances, these lobes partially overlap and form a characteristic Y-shaped pattern, which is typical for binary axicons due to the limited spatial separation between the initial diffraction maxima.

In contrast, the axicon with  $m = 10$  produces a well-resolved multi-lobe ring (Fig. 13(b)), in good agreement with the simulated patterns in Fig. 8. Both axicons exhibit weak spiral-like background features

associated with the binary phase discretization.

Measured power losses did not exceed 30%, indicating high transmission and good mode quality. As the propagation distance increased, the ring radius expanded while the internal lobe structure remained nearly unchanged, consistent with the expected behavior of quasi-Bessel beams with low angular divergence.

Finally, we note that Bessel and quasi-Bessel beams cannot be converted into Hermite-Gaussian modes using a cylindrical-lens scheme, since their propagation-invariant structure does not undergo the conventional LG-to-HG transformation. For such beams, the orbital angular momentum projection simply coincides with the topological charge  $m$ . As shown in Ref. [22],  $m$  can be obtained simply by counting the number of intensity maxima in the ring, providing a straightforward and reliable method for identifying the OAM content of quasi-Bessel beams. In practice, quasi-Bessel beams can exhibit a finite OAM bandwidth due to slight contributions from nearby OAM states, but the average topological charge still corresponds to  $m$ , as discussed in Section 3.

## 5 Discussion and Conclusion

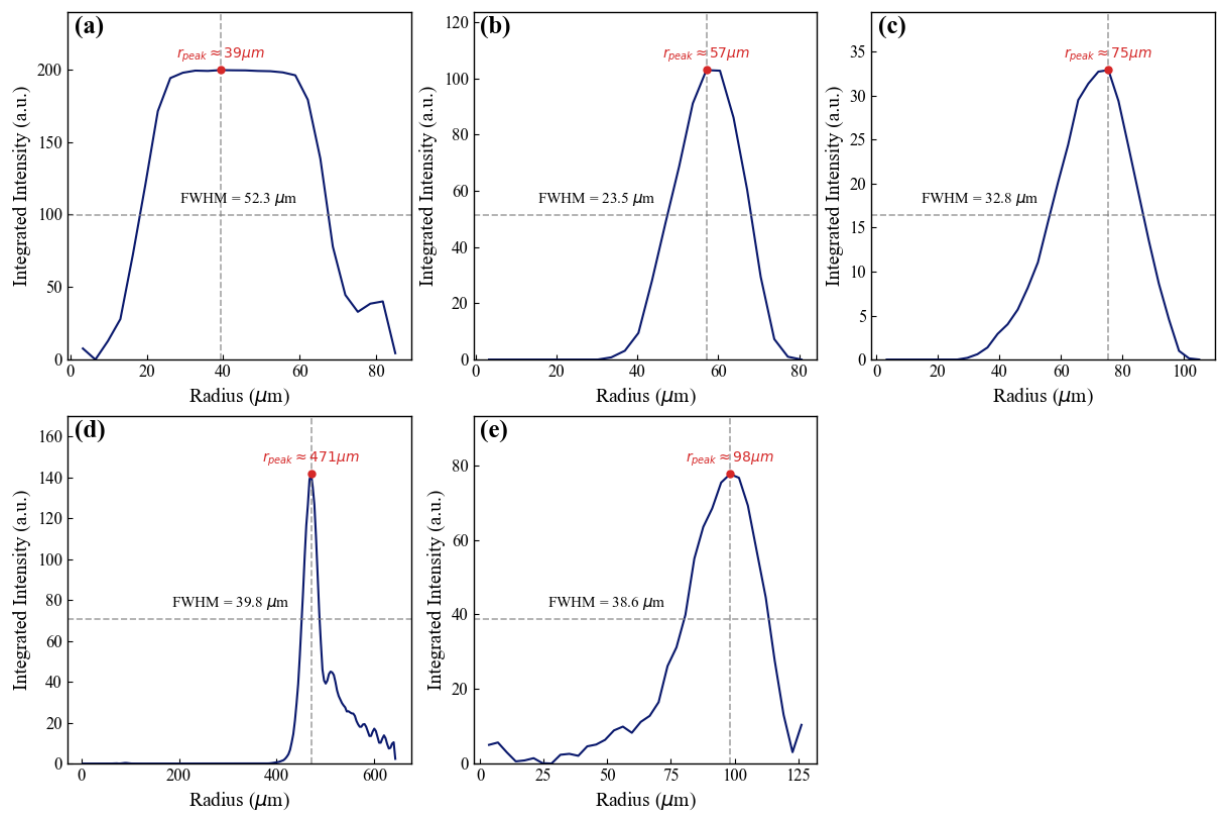


**Figure 14:** Radial profiles of the generated twisted light beams: (a) – (c) – fork grating producing the OAM  $\ell = 2$ ,  $\ell = 4$  and  $\ell = 8$  modes; (d) – SPP generating a high-order LG beam with  $\ell = 64$ ; (e) – binary axicon producing a quasi-Bessel beam with the topological charge  $m = 10$ .

We have demonstrated the generation of high-OAM ultraviolet twisted light using three types of diffractive optical elements: a fork grating, a spiral phase plate, and binary axicons. The fork grating, being the simplest and most cost-effective DOE, produced vortex modes of high quality (Fig. 14(a)–(c)) with well-formed single-ring structures and clear central minima. As discussed in Sec. 4.2, the first ring width reflects the conversion efficiency from the incident Gaussian beam: lower topological charges yield broader rings, while higher charges produce narrower rings that gradually widen with increasing OAM, consistent with LG modal scaling. The ring radius increase systematically with OAM, matching theoretical predictions (Fig. 6).

Measured energy distribution indicates a substantial fraction of power in zeroth and low diffraction orders, limiting overall conversion efficiency. Nevertheless, stable generation of  $\ell = 2$ ,  $\ell = 4$ , and  $\ell = 8$  OAM states with good control of LG modal structure was achieved.

The grating period could be reduced to improve efficiency, but in our setup this is constrained by

the resolution of the laser-engraving system. Fork gratings remain scalable to higher charges ( $m \sim 8\text{--}10$ ), enabling access to  $\ell \sim 10\text{--}20$  in low diffraction orders, making them suitable for semiconductor photocathodes (e.g.,  $\text{Cs}_2\text{Te}$ , GaAs) with high quantum efficiency [41].

The SPP showed the best overall performance. Its radial profile (Fig. 14(d)) exhibits a smooth annular intensity distribution with a deep central minimum and weak secondary rings, confirming excellent modal purity and high conversion efficiency ( $\approx 80\%$ ). This enabled generation of an  $\ell = 64$  beam with well-defined transverse structure suitable for OAM transfer to relativistic electrons and RF-photoinjector diagnostics. Since the divergence of an LG mode scales as  $\sqrt{\ell}$  [8], beamlines intended for high-OAM injection should take into account the correspondingly larger Twiss  $\beta$ -function [42, 43, 44] and transverse emittance. The high modal purity of the SPP beam also facilitates OAM diagnostics using LG–HG conversion with astigmatic optics [45].

Binary axicons produced quasi-Bessel beams with  $\approx 70\%$  efficiency and robust spatial structure. Despite the multi-lobe transverse pattern typical for binary axicons (Fig. 13(a)), clean radial intensity distributions were observed (Fig. 14(e)), in agreement with topological charge  $m = 10$  and numerical simulations in Sec. 3.

For RF-photoinjector implementation with metallic photocathodes, SPPs and axicons are most attractive due to higher efficiency, better modal purity, and superior power handling. All beams exhibit transverse feature sizes of one to several hundred micrometers, enabling high-charge-density, high-brightness electron beams critical for synchrotrons and free-electron lasers. Diffraction on a triangular aperture provides a promising method to determine OAM for quasi-Bessel beams [46], as LG–HG conversion is inapplicable. Table 1 summarizes our key results and recommendations.

**Table 1:** Comparison of parameters for a fork grating, spiral phase plate, and binary axicon.

Parameter	Fork grating	SPP	Axicon
Fabrication complexity	Low	Very high	High
DUV compatibility	Good	Very high	Very high
Efficiency	60%	80%	70%
Cost	Low	Very high	Mid
Mode quality	High	Very high	High

## Acknowledgement

We deeply acknowledge A.A. Bogdanov for the help that made the fabrication of the spiral phase plate possible. We sincerely thank K.V. Cherepanov for invaluable assistance and advice. We are also grateful to S.S. Baturin for helpful discussions and constructive feedback. We additionally thank N.E. Sheremet for assistance with developing the numerical code used to generate the fork-grating phase masks. The axicons were simulated and fabricated at the shared research facility of Siberian Center for Synchrotron and Terahertz Radiation at the basis of the Novosibirsk Free Electron Laser, Budker Institute of Nuclear Physics SB RAS.

This study was supported by the Russian Science Foundation (Project No. 23-62-10026) [1].

## References

- [1] Russian Science Foundation (Project No. 23-62-10026), <https://rscf.ru/en/project/23-62-10026/>.
- [2] L. Allen, M. W. Beijersbergen, R. J. C. Spreeuw, J. P. Woerdman, Orbital angular momentum of light and the transformation of laguerre-gaussian laser modes, *Phys. Rev. A* 45 (1992) 8185–8189. [doi:10.1103/PhysRevA.45.8185](https://doi.org/10.1103/PhysRevA.45.8185).
- [3] D. L. Andrews, M. Babiker, *The Angular Momentum of Light*, 1st Edition, Cambridge University Press, 2012. [doi:10.1017/CB09780511795213](https://doi.org/10.1017/CB09780511795213).
- [4] S. Franke-Arnold, L. Allen, M. Padgett, Advances in optical angular momentum, *Laser & Photonics Reviews* 2 (4) (2008) 299–313. [doi:https://doi.org/10.1002/lpor.200810007](https://doi.org/10.1002/lpor.200810007).

- [5] K. Bliokh, I. Ivanov, G. Guzzinati, L. Clark, R. Van Boxem, A. B  ch  , R. Juchtmans, M. Alonso, P. Schattschneider, F. Nori, J. Verbeeck, Theory and applications of free-electron vortex states, *Physics Reports* 690 (2017) 1–70, theory and applications of free-electron vortex states. doi:<https://doi.org/10.1016/j.physrep.2017.05.006>.
- [6] M. Babiker, D. L. Andrews, V. E. Lembessis, Atoms in complex twisted light, *Journal of Optics* 21 (1) (2018) 013001. doi:[10.1088/2040-8986/aaed14](https://doi.org/10.1088/2040-8986/aaed14).
- [7] K. Floettmann, D. Karlovets, Quantum mechanical formulation of the busch theorem, *Phys. Rev. A* 102 (2020) 043517. doi:[10.1103/PhysRevA.102.043517](https://doi.org/10.1103/PhysRevA.102.043517).
- [8] D. Karlovets, Vortex particles in axially symmetric fields and applications of the quantum busch theorem, *New Journal of Physics* 23 (3) (2021) 033048. doi:[10.1088/1367-2630/abeacc](https://doi.org/10.1088/1367-2630/abeacc).
- [9] I. P. Ivanov, Promises and challenges of high-energy vortex states collisions, *Progress in Particle and Nuclear Physics* 127 (2022) 103987. doi:<https://doi.org/10.1016/j.pnpnp.2022.103987>.
- [10] S. Fu, C. Gao, *Optical Vortex Beams: Fundamentals and Techniques*, 1st Edition, Springer Singapore, 2024. doi:[10.1007/978-981-99-1810-2](https://doi.org/10.1007/978-981-99-1810-2).
- [11] A. Schimmoller, S. Walker, A. S. Landsman, Photonic angular momentum in intense light–matter interactions, *Photonics* 11 (9) (2024). doi:[10.3390/photonics11090871](https://doi.org/10.3390/photonics11090871).
- [12] F. Brandt, M. Hiekkam  ki, F. Bouchard, M. Huber, R. Fickler, High-dimensional quantum gates using full-field spatial modes of photons, *Optica* 7 (2) (2020) 98–107. doi:[10.1364/OPTICA.375875](https://doi.org/10.1364/OPTICA.375875).
- [13] R. Fickler, F. Bouchard, E. Giese, V. Grillo, G. Leuchs, E. Karimi, Full-field mode sorter using two optimized phase transformations for high-dimensional quantum cryptography, *Journal of Optics* 22 (2) (2020) 024001. doi:[10.1088/2040-8986/ab6303](https://doi.org/10.1088/2040-8986/ab6303).
- [14] H. Cao, S.-C. Gao, C. Zhang, J. Wang, D.-Y. He, B.-H. Liu, Z.-W. Zhou, Y.-J. Chen, Z.-H. Li, S.-Y. Yu, J. Romero, Y.-F. Huang, C.-F. Li, G.-C. Guo, Distribution of high-dimensional orbital angular momentum entanglement over a 1-km few-mode fiber, *Optica* 7 (3) (2020) 232–237. doi:[10.1364/OPTICA.381403](https://doi.org/10.1364/OPTICA.381403).
- [15] A. Deno  ud, L. Chopineau, A. Leblanc, F. Qu  r  , Interaction of ultraintense laser vortices with plasma mirrors, *Phys. Rev. Lett.* 118 (2017) 033902. doi:[10.1103/PhysRevLett.118.033902](https://doi.org/10.1103/PhysRevLett.118.033902).
- [16] I. I. Pavlov, A. D. Chaikovskaia, D. V. Karlovets, Generation of vortex electrons by atomic photoionization, *Phys. Rev. A* 110 (2024) L031101. doi:[10.1103/PhysRevA.110.L031101](https://doi.org/10.1103/PhysRevA.110.L031101).
- [17] A. S. Dyatlov, M. A. Nozdrin, A. N. Sergeev, N. E. Sheremet, S. S. Stafeev, D. V. Karlovets, Generation of deep ultraviolet vortices via amplitude and phase spiral zone plates, *Appl. Opt.* 64 (36) (2025) 10776–10780. doi:[10.1364/AO.578189](https://doi.org/10.1364/AO.578189).
- [18] A. I. Solomonov, O. M. Kushchenko, K. I. Kasyanova, S. B. Isaeva, I. I. Shishkin, D. Y. Terekhov, P. I. Lazarenko, M. V. Rybin, S. S. Baturin, A. D. Sinelnik, Switching topological charge of optical vortex by two-dimensional structures, *Applied Materials Today* 37 (2024) 102135. doi:[10.1016/j.apmt.2024.102135](https://doi.org/10.1016/j.apmt.2024.102135).
- [19] S. N. Khonina, V. V. Podlipnov, S. V. Karpeev, A. V. Ustinov, S. G. Volotovskiy, S. V. Ganchevskaya, Spectral control of the orbital angular momentum of a laser beam based on 3d properties of spiral phase plates fabricated for an infrared wavelength, *Opt. Express* 28 (12) (2020) 18407–18417. doi:[10.1364/OE.396199](https://doi.org/10.1364/OE.396199).
- [20] S. S. R. Oemrawsingh, J. A. W. van Houwelingen, E. R. Eliel, J. P. Woerdman, E. J. K. Verstegen, J. G. Kloosterboer, G. W. ’t Hooft, Production and characterization of spiral phase plates for optical wavelengths, *Appl. Opt.* 43 (3) (2004) 688–694. doi:[10.1364/AO.43.000688](https://doi.org/10.1364/AO.43.000688).
- [21] N. Osintseva, V. Gerasimov, B. Knyazev, M. Komlenok, V. Pavelyev, D. Yablokov, Terahertz bessel and ”perfect” vortex beams generated with a binary axicon and axicon with continuous relief, *Computer Optics* 3 (46) (2022) 375–380. doi:[10.18287/2412-6179-CO-1066](https://doi.org/10.18287/2412-6179-CO-1066).

- [22] B. Knyazev, N. Osintseva, M. Komlenok, V. Pavelyev, V. Gerasimov, O. Kameshkov, Y. Choporova, K. Tukmakov, Terahertz Bessel beams formed by binary and holographic axicons, *Photonics* 10 (6) (2023). doi:[10.3390/photonics10060700](https://doi.org/10.3390/photonics10060700).
- [23] N. Bazdyrev, V. Gerasimov, V. Pavelyev, A. Agafonov, K. Tukmakov, Techniques to estimate zone of formation of terahertz Bessel vortex beams, *Journal of Infrared, Millimeter, and Terahertz Waves* 47 (46) (2025). doi:[10.1007/s10762-025-01066-4](https://doi.org/10.1007/s10762-025-01066-4).
- [24] E. I. Gacheva, A. K. Poteomkin, E. A. Khazanov, V. V. Zelenogorskii, E. V. Katin, G. A. Luchinin, N. I. Balalykin, V. F. Minashkin, M. A. Nozdryn, G. V. Trubnikov, G. D. Shirkov, Laser driver for a photoinjector of an electron linear accelerator, *IEEE Journal of Quantum Electronics* 50 (7) (2014) 522–529. doi:[10.1109/JQE.2014.2323472](https://doi.org/10.1109/JQE.2014.2323472).
- [25] P. Schattschneider, B. Schaffer, I. Ennen, J. Verbeeck, Mapping spin-polarized transitions with atomic resolution, *Phys. Rev. B* 85 (2012) 134422. doi:[10.1103/PhysRevB.85.134422](https://doi.org/10.1103/PhysRevB.85.134422).
- [26] Y. Wu, L. Ji, X. Geng, Q. Yu, N. Wang, B. Feng, Z. Guo, W. Wang, C. Qin, X. Yan, L. Zhang, J. Thomas, A. Hützen, M. Büscher, T. P. Rakitzis, A. Pukhov, B. Shen, R. Li, Polarized electron-beam acceleration driven by vortex laser pulses, *New Journal of Physics* 21 (7) (2019) 073052. doi:[10.1088/1367-2630/ab2fd7](https://doi.org/10.1088/1367-2630/ab2fd7).
- [27] F. An, D. Bai, H. Cai, S. Chen, X. Chen, H. Duyang, L. Gao, S. Ge, J. He, J. Huang, Z. Huang, I. Ivanov, C. Ji, H. Jia, J. Jiang, X. Kang, S.-B. Kim, C. Kong, W. Kou, Q. Li, Q. Li, J. Liao, J. Ling, C.-E. Liu, X. Ma, H. Qiu, J. Tang, R. Wang, W. Wen, J. Wu, J. Xiao, X. Xiao, Y. Xu, W. Yang, X. Yang, J. Yao, Y. Yuan, M. Zaiba, P. Zhang, S. Zhang, S. Zhang, S. Zhao, L. Zou, High-precision physics experiments at huizhou large-scale scientific facilities, *Chinese Physics Letters* 42 (11) (2025) 110102. doi:[10.1088/0256-307X/42/11/110102](https://doi.org/10.1088/0256-307X/42/11/110102).
- [28] V. V. Kotlyar, A. A. Kovalev, A. G. Nalimov, *Topological Charge of Optical Vortices*, 1st Edition, Taylor & Francis Group, 2022. doi:[10.1201/9781003326304](https://doi.org/10.1201/9781003326304).
- [29] B. Goebel, L. L. Wang, T. Tschudi, Multilayer technology for diffractive optical elements, *Appl. Opt.* 35 (22) (1996) 4490–4493. doi:[10.1364/AO.35.004490](https://doi.org/10.1364/AO.35.004490).
- [30] X. Wang, J. R. Leger, R. H. Rediker, Rapid fabrication of diffractive optical elements by use of image-based excimer laser ablation, *Appl. Opt.* 36 (20) (1997) 4660–4665. doi:[10.1364/AO.36.004660](https://doi.org/10.1364/AO.36.004660).
- [31] G. Kostyuk, V. Shkuratova, A. Petrov, D. Mesheryakov, K. Eliseev, D. Stepanyuk, Multisector binary phase plates on fused silica for generation of optical vortex beams superposition: Fabrication, characterization, and applications, *Optics & Laser Technology* 152 (2022) 108161. doi:<https://doi.org/10.1016/j.optlastec.2022.108161>.
- [32] C. Shi, W. Zhao, S. Chen, W. Li, Multilevel diffractive lenses: Recent advances and applications, *Symmetry* 16 (10) (2024). doi:[10.3390/sym16101377](https://doi.org/10.3390/sym16101377).
- [33] O. E. Kameshkov, B. A. Knyazev, Simulating diffraction on a series of amplitude-phase masks for experiments at the Novosibirsk free electron laser, *Bulletin of the Russian Academy of Sciences: Physics* 83 (2) (2019) 184–189. doi:[10.3103/S1062873819020175](https://doi.org/10.3103/S1062873819020175).
- [34] J. Goodman, *Introduction to Fourier optics*, 3rd Edition, Roberts & Co. Publishers, 2005.
- [35] V. Nazmov, E. Reznikova, J. Mohr, A. Snigirev, I. Snigireva, S. Achenbach, V. Saile, Fabrication and preliminary testing of x-ray lenses in thick SU-8 resist layers, *Microsystem Technologies* 10 (10) (2004) 716–721. doi:[10.1007/s00542-004-0433-0](https://doi.org/10.1007/s00542-004-0433-0).
- [36] R. Vasilyeu, A. Dudley, N. Khilo, A. Forbes, Generating superpositions of higher-order Bessel beams, *Opt. Express* 17 (26) (2009) 23389–23395. doi:[10.1364/OE.17.023389](https://doi.org/10.1364/OE.17.023389).
- [37] A. A. Kovalev, V. V. Kotlyar, A. P. Porfirev, Shifted nondiffractive Bessel beams, *Phys. Rev. A* 91 (2015) 053840. doi:[10.1103/PhysRevA.91.053840](https://doi.org/10.1103/PhysRevA.91.053840).
- [38] F. Saadati-Sharafteh, A. Borhanifar, A. P. Porfirev, P. Amiri, E. A. Akhlaghi, S. N. Khonina, Y. Azizian-Kalandaragh, The superposition of the Bessel and mirrored Bessel beams and investigation of their self-healing characteristic, *Optik* 208 (2020) 164057. doi:<https://doi.org/10.1016/j.ijleo.2019.164057>.

- [39] M. Beijersbergen, L. Allen, H. van der Veen, J. Woerdman, Astigmatic laser mode converters and transfer of orbital angular momentum, *Optics Communications* 96 (1) (1993) 123–132. doi:[10.1016/0030-4018\(93\)90535-D](https://doi.org/10.1016/0030-4018(93)90535-D).
- [40] V. V. Kotlyar, A. A. Kovalev, A. P. Porfirev, Astigmatic transforms of an optical vortex for measurement of its topological charge, *Appl. Opt.* 56 (14) (2017) 4095–4104. doi:[10.1364/AO.56.004095](https://doi.org/10.1364/AO.56.004095).
- [41] R. Xiang, J. Teichert, Photocathodes for high brightness photo injectors, *Physics Procedia* 77 (2015) 58–65, international Conference on Laser Applications at Accelerators, LA3NET 2015, 25-27 March 2015, Mallorca, Spain. doi:[10.1016/j.phpro.2015.11.010](https://doi.org/10.1016/j.phpro.2015.11.010).
- [42] H. Wiedemann, *Particle Accelerator Physics*, 4th Edition, Springer Cham, 2015. doi:[10.1007/978-3-319-18317-6](https://doi.org/10.1007/978-3-319-18317-6).
- [43] A. W. Chao, *Lectures on Accelerator Physics*, 1st Edition, World Scientific, 2020. doi:[10.1142/12004](https://doi.org/10.1142/12004).
- [44] S. Y. Lee, *Accelerator Physics*, 4th Edition, World Scientific Publishing Company, 2021. doi:[10.1142/11111](https://doi.org/10.1142/11111).
- [45] P. Schattschneider, M. Stöger-Pollach, J. Verbeeck, Novel vortex generator and mode converter for electron beams, *Phys. Rev. Lett.* 109 (2012) 084801. doi:[10.1103/PhysRevLett.109.084801](https://doi.org/10.1103/PhysRevLett.109.084801).
- [46] M. Maksimov, N. Borodin, D. Kargina, D. Naumov, D. Karlovets, Diffraction by circular and triangular apertures as a diagnostic tool of twisted matter waves (2025). [arXiv:2510.00826](https://arxiv.org/abs/2510.00826).